European Journal of Mechanics / A Solids 112 (2025) 105609

Contents lists available at ScienceDirect

European Journal of Mechanics / A Solids

journal homepage: www.elsevier.com/locate/ejmsol

Full length article

Analysis of a prismatic elastic contact of finite length

Yifeng Chen [a], David A. Hills [a], John E. Huber [a,*], Lifeng Ma [b]

[a] Department of Engineering Science, University of Oxford, Parks Road, OX1 3PJ Oxford, UK
[b] S&V Lab, Department of Engineering Mechanics, Xi'an Jiaotong University, 710049 Xi'an, China

ARTICLE INFO

Keywords:
Contact of finite length
Finite element analysis
End effects
Saint-Venant's principle

ABSTRACT

This paper is concerned with a contact problem which is geometrically two dimensional, but of finite extent in a third dimension. Two different contact models (common edge contact and incomplete contact) are analyzed, using a finite element model to investigate the 3D end effects. The object is to take the 2D plane strain solution in each model as a reference, and to show how it must be modified to allow for the 3D finite extent contact problem with free end faces. It is shown that, for a sufficiently long prismatic contact, the in-plane stress distribution at the mid-plane matches the solution to the 2D plane strain problem. Additionally, the end effect is evaluated using the finite element results to show how it decays with distance from the free end. The decay is exponential and governed by a dominant length-scale of the problem. For a common edge contact, this length-scale is the contact width. However, for a Hertzian contact, the contact width varies in the third dimension and the governing length scale is the radius of curvature, typically much larger than the contact width.

1. Introduction

Prismatic elastic contacts of finite length are frequently found in engineered components, including splined shafts, gears and turbine blade roots. In order to gain a general understanding of such contacts, a two-dimensional (2D) analysis may be used. However, all such contacts in practice have ends, and the end effects may significantly influence contact pressure. There is thus a requirement to understand how the solution of prismatic contact problems differs from the solution to a corresponding 2D problem. This difference defines an end-correction that decays away towards the mid-plane of the contact. An interesting feature of the problem, as will be shown in this paper, is that the end-correction can propagate far into the contact. This is especially relevant to the Hertzian contact between cylinders, where, as will be shown, the relevant length scale for propagation of the end-correction is the radius of curvature at the contact.

One way to observe the end effect in prismatic contacts is by conducting fretting tests, where it is found that the contact or wear scar varies in the through-thickness direction, despite prismatic component geometry (Blades et al., 2023). Fretting tests commonly employ pads pressed into a traditional dog-bone-shaped tensile test specimen, as shown in Fig. 1 (see also Truelove et al., 2023; De Pannemaecker et al., 2018). These tests aim to reveal the fretting fatigue strength of the material. The pads have prismatic geometry with a cross-section that may be either flat-and-rounded in form or circular. A significant amount of effort has been invested in analyzing the behavior of these contacts in partial slip. The analysis has commonly been conducted under plane conditions, i.e. where there are no permitted gradients of stress or strain components in the out-of-plane direction. The tests themselves are intended to match these conditions: care is taken to use pads of prismatic geometry, and to match the through-thickness length of the pads to the width of the dog-bone specimen. However, it is inevitable that there are deviations from prismatic contact conditions due to imperfection and the nature of incomplete contact. The singular solution due to slight mismatch of through-thickness length typically has little effect in practical experimental conditions. By contrast, the end effect due to the free surfaces can intrude far into the contact, making it essential to account for this effect. The objective of the current work is to analyze the end effect due to the free surfaces at the ends of prismatic contacts.

The structure of the paper is as follows: first, general properties of prismatic contacts are considered and it is shown that the elastic fields can be decomposed into those due to bodies constrained in plane strain and an additional set of corrective fields due to the end effect. Then, particular geometries are explored. The target problem is a Hertzian contact in which a cylinder is pressed against a flat surface. However, this problem is complicated by the non-prismatic contact profile that forms when the cylinders are pressed together. For this reason, a common edge contact problem in which symmetric anvils are pressed together is first explored. This has the advantage that the problem

* Corresponding author.
E-mail address: john.huber@eng.ox.ac.uk (J.E. Huber).

https://doi.org/10.1016/j.euromechsol.2025.105609
Received 16 September 2024; Received in revised form 4 February 2025; Accepted 7 February 2025
Available online 14 February 2025

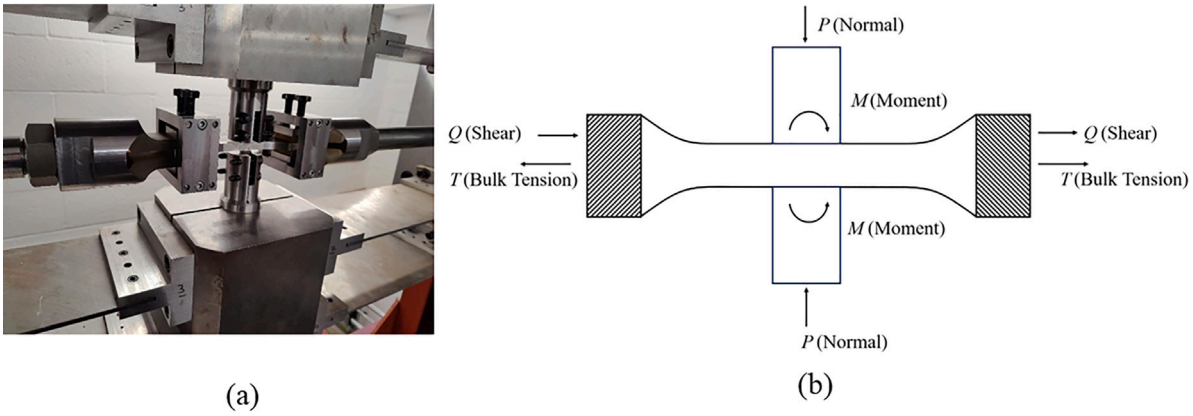

Fig. 1. (a) Experimental apparatus for fretting tests. (b) Idealization of the key part of the test.

geometry defines the contact width; combined with symmetry, a result is that the elastic pair can be treated as a monolithic body, which is computationally efficient to model while revealing key features of the problem. The analysis uses the finite element method for a 3D evaluation of stress fields and compares the results with a 2D plane strain solution. The decay-rate of the end-effects is evaluated for both Hertzian and common-edge contacts, and it is shown that this follows an oscillatory exponential decay, typical of the Saint-Venant decay for end effects. A detailed comparison between the Hertzian contact and the common-edge contact is given.

2. Theoretical background

2.1. Prismatic body with uniform loading

We begin by examining a monolithic and homogeneous prismatic body of arbitrary cross section, with length $2L$ much greater than the leading dimension of the cross-section. The body is elastic and is subjected to a uniform distributed normal force P and shear force Q per unit length. This body is additionally constrained by fixed frictionless planes at $z = 0$ and $z = L$, such that the through-thickness displacement u_z is zero everywhere, as depicted in Fig. 2(a). The condition $u_z = 0$ effectively ensures that each cross-sectional plane along its length satisfies the plane strain condition, i.e. $\epsilon_{zz} = 0$ everywhere, thereby maintaining an identical in-plane stress state in all of these cross-sections. In addition to the applied loads P and Q, the geometry shown in Fig. 2(a) sustains a non-uniform stress distribution perpendicular to the x-y plane, $\sigma^{\mathrm{PS}}_{zz}(x, y)$, where the superscript PS stands for plane strain. This ensures that the through-thickness strain components ϵ_{zz} vanish. The distribution of $\sigma^{\mathrm{PS}}_{zz}(x, y)$ is characterized by:

$$\sigma^{\mathrm{PS}}_{zz}(x, y) = \nu(\sigma^{\mathrm{PS}}_{xx}(x, y) + \sigma^{\mathrm{PS}}_{yy}(x, y)) \tag{1}$$

where ν is Poisson's ratio. By considering the applied loads P and Q and the stress $\sigma^{\mathrm{PS}}_{zz}(x, y)$ separately, the plane strain case can be decomposed into two parts. The first part is the target problem, defined by a prismatic body loaded by P and Q, of finite extent, with both ends being free, as shown in Fig. 2(b). The second part is a corrective solution defined by the same body, loaded with the plane strain through-thickness stress, as illustrated in Fig. 2(c). Note that the target problem is a classic prismatic bar problem, and the analytical solution is discussed in Barber (2006) using Papkovich–Neuber solution. This solution will not be applied in this paper due to its mathematical complexity. Instead, the superposition principle is applied to illustrate the stress state behavior.

We refer to the problem shown in Fig. 2(b) as the 'finite length problem', which is found in many practical situations. In the corrective solution, σ_{zz} varies with position (x, y, z), but the variation in the x-y plane decays with distance z along the length, according to Saint-Venant's principle (Love, 2013). Since σ_{zz} has a non-zero average over the x-y plane, and may have a non-zero net moment if the plane geometric shape is not symmetrical about z−plane, this stress field decays towards the average stress plus the stress generated by the net moment as the center $(z = L)$ is approached, if L is sufficiently large. Generally, the corrective solution decays away over a transition region the size of which will be evaluated later in the paper.

Let σ^{a}_{zz} be the average of stress $\sigma^{\mathrm{PS}}_{zz}(x, y)$ over the x-y plane, given by:

$$\sigma^{\mathrm{a}}_{zz} = \frac{1}{A_0}\int_{A_0} \sigma^{\mathrm{PS}}_{zz}(x, y)\,\mathrm{d}A \tag{2}$$

where A_0 is the cross-sectional area of the prismatic body. Let M be the net moment, I be the second moment of area and y_{n} be the y-coordinate of the neutral axis, the stress generated by the net moment, $\sigma^{\mathrm{M}}(y)$, on the mid-plane is given by:

$$\sigma^{\mathrm{M}}_{zz}(y) = \frac{M(y - y_{\mathrm{n}})}{I} \tag{3}$$

Also define $\sigma^{\mathrm{b}}_{zz}(x, y)$ as the self-balancing complementary stress field given by

$$\sigma^{\mathrm{PS}}_{zz}(x, y) = \sigma^{\mathrm{b}}_{zz}(x, y) + \sigma^{\mathrm{a}}_{zz} + \sigma^{\mathrm{M}}_{zz}(y). \tag{4}$$

Then, according to Saint-Venant's principle, $\sigma_{zz}(x, y, z)$ in the corrective solution, makes a transition from $\sigma^{\mathrm{b}}_{zz}(x, y)+\sigma^{\mathrm{a}}_{zz}+\sigma^{\mathrm{M}}_{zz}(y)$ at the ends of the prismatic body, to $\sigma^{\mathrm{a}}_{zz}+\sigma^{\mathrm{M}}_{zz}(y)$ at $z = L$. The propagation of $\sigma_{zz}(x, y, z)+\sigma^{\mathrm{a}}_{zz} + \sigma^{\mathrm{M}}_{zz}(y)$ is illustrated in Fig. 3, which shows a non-uniformly distributed stress gradually changes to a uniformly distributed stress at the mid-plane plus the stress generated by the net moment, if L is sufficiently large. The decay of the zero-resultant stress σ^{b}_{zz} is the free end-effect investigated in this paper. The region of this decay is typically short compared to the length $2L$. Hence there is a transient region, wherein the stress state is dependent on the z co-ordinate, followed by a steady-state region, where no end-effect is present and the stress state is practically constant along the z-axis.

The mid-plane is of particular interest, because it is guaranteed to remain plane in the loaded state, due to symmetry. Also, it represents the steady-state behavior beyond the transient region. Noting the superposition shown in Fig. 2, the mid-plane stress field is given by subtracting σ^{a}_{zz} from the plane strain solution. Therefore, the stress field at the mid-plane σ^{m}_{ij} (also the entire steady state region)can be expressed as:

$$\sigma^{\mathrm{m}}_{ij} = \sigma^{\mathrm{PS}}_{ij} \quad \text{for } i, j \in \{x, y\}, \tag{5}$$

$$\sigma^{\mathrm{m}}_{zz} = \sigma^{\mathrm{PS}}_{zz} - \sigma^{\mathrm{a}}_{zz} - \sigma^{\mathrm{M}}_{zz}(y) = \sigma^{\mathrm{b}}_{zz}, \tag{6}$$

$$\sigma^{\mathrm{m}}_{xz} = \sigma^{\mathrm{m}}_{yz} = 0. \tag{7}$$

Note that the in-plane stress fields σ^{m}_{xx}, σ^{m}_{yy} and σ^{m}_{xy} are the same as those calculated in the plane strain condition.

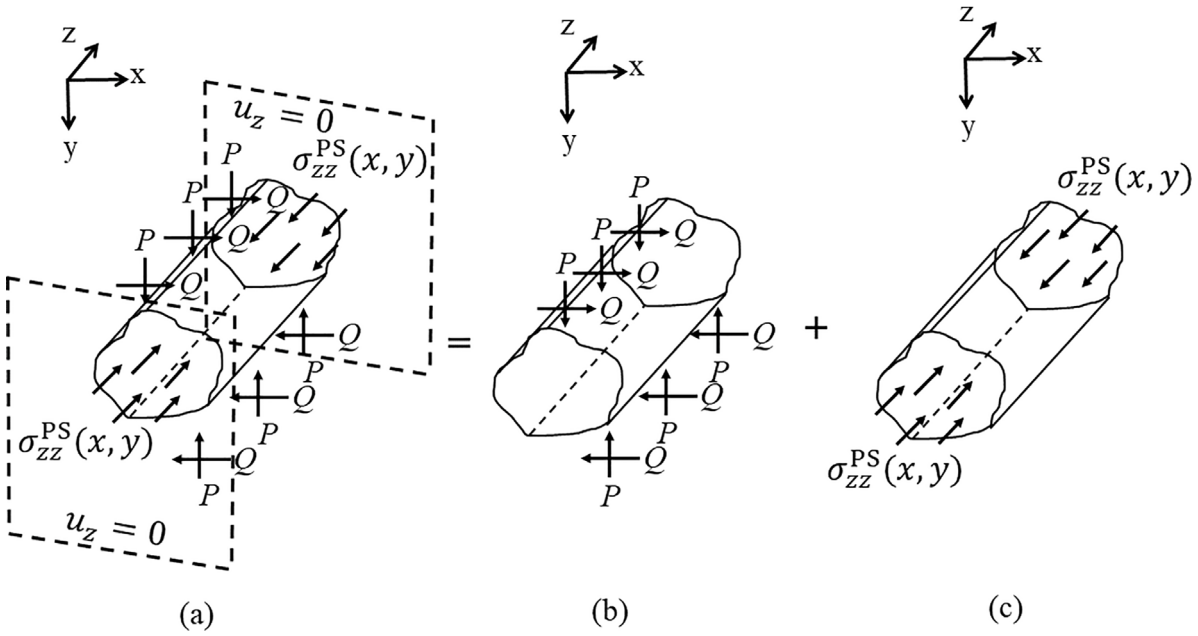

Fig. 2. An arbitrary prismatic body of finite length (a) loaded by applied loads P and Q in plane strain; (b) loaded by applied loads P and Q with free ends (our target); (c) loaded by the through-thickness stress $\sigma_{zz}^{PS}(x,y)$ (corrective solution).

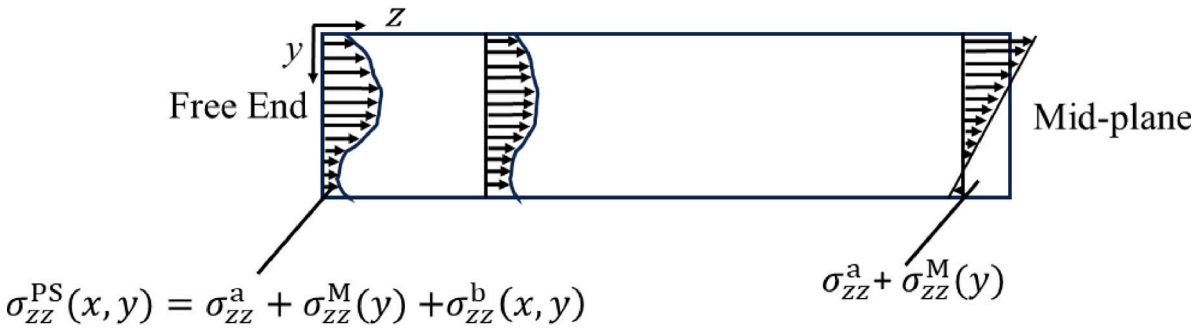

Fig. 3. Illustration of the propagation of $\sigma_{zz}(x,y,z)$ in the corrective solution, from the non-uniform distribution $\sigma_{zz}^{PS}(x,y)$ at the free-end to a uniform distribution at the mid-plane σ_{zz}^{a}.

2.2. Prismatic contact problem

Next, consider a contact made by two prismatic bodies of the same length, $2L$, where $2L$ is much larger than the leading dimension of the cross section of the prismatic body, under uniform load. The conclusion that the in-plane components of σ^{m} equal those of σ^{PS} may not hold in this problem. This is because, firstly, the contact pressure may vary with the z co-ordinate in a contact problem: thus the requirement that the loading is independent of z may not be satisfied. Secondly, the contact pressure, especially in incomplete contact, is not linearly related to the applied load; thus, strictly, the principle of superposition is invalid and Eqs. (5)–(7) are not applicable.

Nevertheless, if we impose the corrective stress field, $-\sigma_{zz}^{PS}(x,y)$, at both ends of a prismatic contact under plane strain condition, then a finite length contact problem is constructed because of the match of the free-end boundary conditions, as depicted in Fig. 4, using a Hertzian contact as an example. In this case, the stress field at the mid-plane of the finite length contact problem can be evaluated by using two cases: The first case is the prismatic contact under plane strain: here the stress distribution across any plane along the length will be the same as that in the plane strain analytical solution, since the through-thickness displacement, $u_z(x,y)$, is zero in every plane. The second case is the corrective stress added at the both ends, which will be governed by Saint-Venant's principle. This means that there is still a decaying end-effect and the stress state at the mid-plane is equivalent to a uniform stress distribution $-\sigma_{zz}^{a}$ plus the stress $-\sigma_{zz}^{M}(y)$ induced by net the moment imposed on a plane strain contact. The stress distribution on the mid-plane can also be considered representative of the behavior across all planes within the steady-state region.

Therefore, the contact pressure at the mid-plane can be calculated analytically by making use of the plane strain Flamant solution, with an additional out-of-plane stress $-\sigma_{zz}^{a} - \sigma_{zz}^{M}(y)$. Linear superposition can then be used to construct the solution for a general contact pressure distribution. Considering first this problem, the in-plane stress field in Cartesian coordinates is identical to the Flamant solution and the through-thickness stress component is expressed as:

$$\sigma_{zz}(x,y) = \nu(\sigma_{xx}(x,y) + \sigma_{yy}(x,y)) - \sigma_{zz}^{a} - \sigma_{zz}^{M}(y). \tag{8}$$

The corresponding strains can be computed using Hooke's law. Then, using Flamant's solution with a distributed normal load $p(\xi)\mathrm{d}\xi$ and a distributed shear load $q(\xi)\mathrm{d}\xi$ (here ξ is the x-coordinate for the load) the relative displacement gradients at the mid-plane can be deduced.

If we introduce contacting bodies 1 and 2, with material properties E_1, ν_1 and E_2, ν_2, the relative surface vertical displacement $h(x)$ and the relative surface horizontal displacement $g(x)$ can then be expressed as:

$$\frac{1}{\alpha}\frac{\partial h}{\partial x} = -\frac{1}{\pi}\int \frac{p(\xi)d\xi}{x-\xi} - \beta q(x) \tag{9}$$

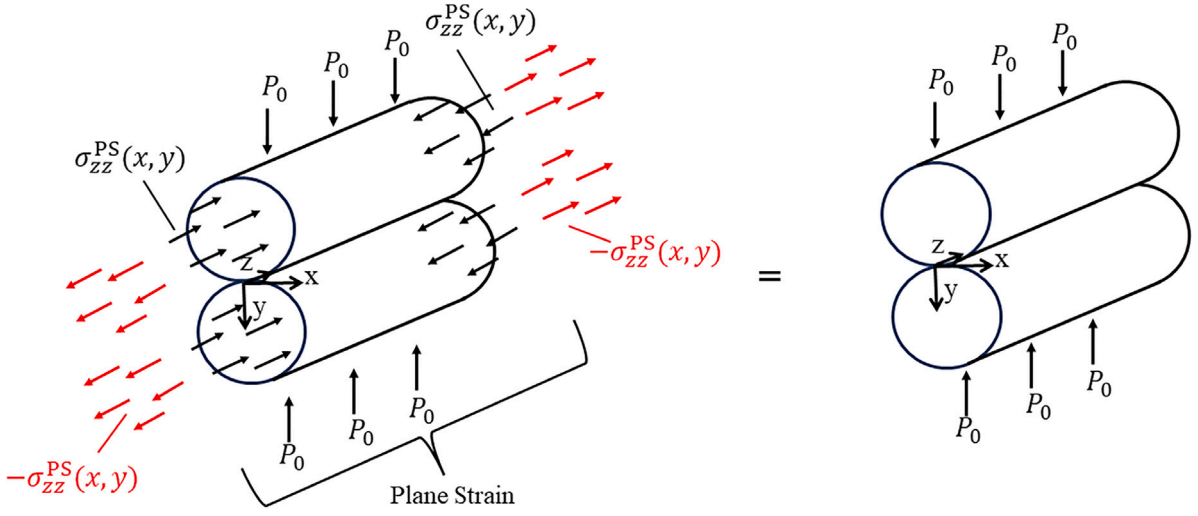

Fig. 4. Illustration of the finite length contact problem, constructed by imposing the corrective stress field, $-\sigma_{zz}^{PS}(x,y)$ (indicated in red) onto a prismatic contact under plane strain. (For interpretation of the references to color in this figure legend, the reader is referred to the web version of this article.)

$$\frac{1}{\alpha}\frac{\partial g}{\partial x} = -\frac{1}{\pi}\int \frac{q(\xi)d\xi}{x-\xi} + \beta p(x) + \gamma(\sigma_{zz}^{a} + \sigma_{zz}^{M}(y)) \tag{10}$$

where

$$\alpha = 2\left[\frac{(1-\nu_1^2)}{E_1} + \frac{(1-\nu_2^2)}{E_2}\right]$$

refers as the composite compliance and

$$\beta = \frac{\frac{(1+\nu_1)(1-2\nu_1)}{E_1} - \frac{(1+\nu_2)(1-2\nu_2)}{E_2}}{\frac{(1-\nu_1^2)}{E_1} + \frac{(1-\nu_2^2)}{E_2}}$$

refers as the Dundurs' second constant and

$$\gamma = \frac{\nu_1}{E_1} - \frac{\nu_2}{E_3}.$$

Eqs. (9) and (10) show the displacement gradient at the contact interface for the mid-plane of the finite length contact problem, and the only difference compared with those in a plane strain contact solution is the additional $\gamma(\sigma_{zz}^{a} + \sigma_{zz}^{M}(y))$ in the horizontal displacement gradient (see Hills et al., 2013; Johnson, 1987 for plane strain displacement gradients). There are special cases in which Eqs. (9) and (10) are uncoupled, i.e., $\beta = 0$ or $q(x) = 0$. Another special case arises when the two contacting bodies have the same $\frac{\nu}{E}$ ratio, i.e., $\gamma = 0$. In these cases we can expect that at the mid-plane, the contact pressure $p(x)$ will be the same as that in the plane strain solution, provided the contact is long enough.

The theoretical analysis provides insight into the problem, but some aspects remain unknown, such as how far the free end effect penetrates along the length direction and what the decay pattern of this free end effect is. Two finite element experiments related to the contact problem are next conducted to further explore these aspects and to validate the theoretical findings. To reduce computational effort, the chosen plane geometric shape will be symmetrical about the z-plane for finite element experiments; therefore, we do not consider any net moment involvement.

3. Finite length, common-edge contact

The eventual objective is to solve the problem of a Hertzian contact between uniformly loaded, elastically similar cylinders of finite length. The degree of lateral constraint in this problem varies: at the mid-plane the through-thickness displacement is zero, whereas at the free ends, the tractions σ_{zz}, σ_{zx} and σ_{zy} must vanish over all values of (x, y). The contact patch is not rectangular, complicating the problem significantly. Therefore, as a preliminary exercise, we propose to examine a problem where this feature is absent, namely a common-edge contact between symmetric anvils.

A suitable common-edge contact problem is shown in Fig. 5(a), which depicts two identical, filleted, flat-ended, frictionless anvils, each having a length of $2L$. The anvils are pressed together by a uniformly distributed line force of magnitude P_0 per unit length. For convenience, the height and width of the cross-section are chosen to be the same, denoted as $2w$. The value of w is required to be greater than twice the radius of the fillet, denoted as r, in order to ensure a moderate pressure gradient along the x direction in the contact. Thus the contact half-with is equal to $a = w - r > r$. This is also convenient for finite element mesh construction. Additionally, we require $L \gg w$, so that the end effect will fully decay within the length of the anvils.

The choice of this common edge contact was made in preference to alternatives such as a convex (incomplete or non-conformal) contact of any profile or a complete (conformal) contact of finite width pressed onto a wider block. This is because any prismatic incomplete contact would display the non-constant contact width phenomenon we wish to isolate. Therefore the contact problem would not be prismatic in the deformed state. Meanwhile, a complete contact between blocks of different widths would show a singular edge contact pressure, and this, too, obscures some of the key features of the problem. The chosen contact is defined by both bodies simultaneously, depicted in Fig. 5(c), and has finite contact pressure everywhere; pressure gradients are modest, and the effects of differing degrees of axial constraint are isolated from other features. Because the bodies are identical it follows that no out-of-plane shear tractions σ_{zx}, or σ_{zy}, will arise at any point. Indeed, because the interfacial traction is everywhere compressive it follows that a monolithic finite element model of the pair may be studied, avoiding the need for explicit representation of a contact. The combined geometry is familiar, comprising symmetric semicircular notches in a rectangular section; stress concentration factors are typically less than 2.75 and are available in standard tables (Roark, 1975).

The commercial finite element (FE) package Abaqus FEA was used to analyze the end effect and also validate the results of the theoretical analysis. Using symmetry, only one-eighth of the full geometry was represented in the numerical model. The geometry and loading of the FE model are depicted in Fig. 5(b). Three different sets of numerical experiments with constant width $w = 10\,\text{mm}$ but varying length $L \geq 10w$ and varying characteristic radius r have been examined, see Table 1. The model codes shown in Table 1 are used subsequently to refer to each model.

A finite element model was constructed using 8-node hexahedral elements (C3D8 in Abaqus) with a structured mesh refined near the

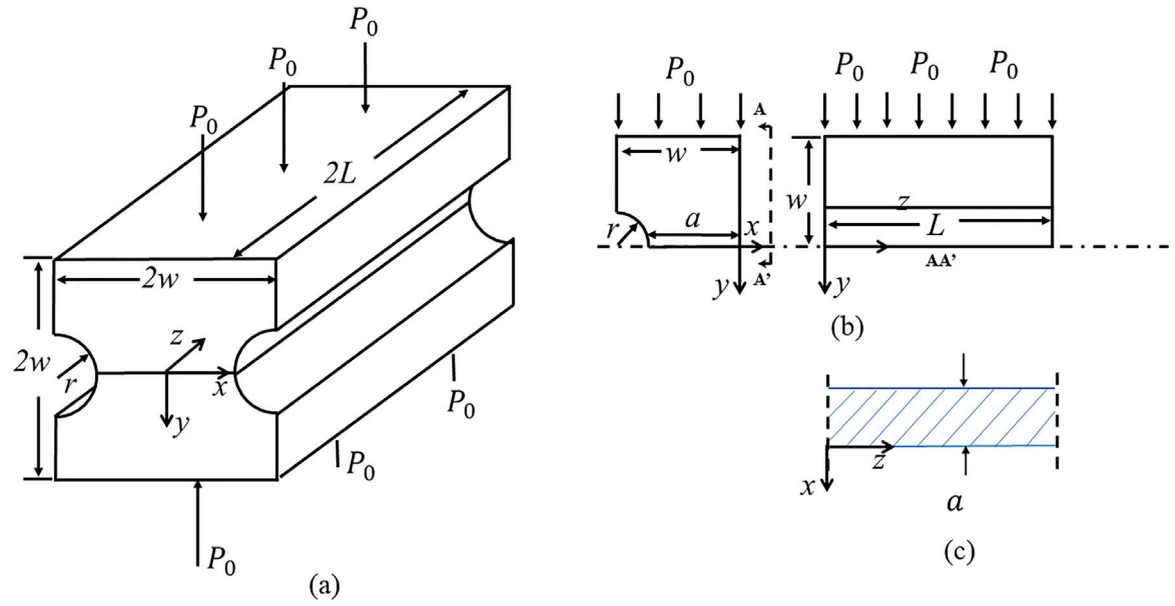

Fig. 5. (a) Finite length, common edge contact, (b) finite element model of finite length, common edge contact, (c) contact half-width distribution for the finite length, common edge contact.

Table 1
FE models with different parameters for finite length, common edge contact: P_0 is the load per unit length, L is the half-length, r is the fillet radius and a is the contact half-width.

Common edge models; $w = 10$ mm				
Model code	P_0 [MPa mm]	L [mm]	r [mm]	a [mm]
P2000L100r2.5a7.5	2000	100	2.5	7.5
P2000L200r2.5a7.5	2000	200	2.5	7.5
P2000L100r5a5	2000	100	5	5

contact region to accurately capture the stress distribution. The material was assumed to be an isotropic elastic solid, with a Young's modulus of $E = 210$ GPa and a Poisson's ratio of $\nu = 0.3$. Symmetry boundary conditions and frictionless contact were applied, and the model was solved using a static implicit approach to ensure stability. To verify the reliability of the results, a mesh sensitivity study was performed with varying mesh resolutions. This showed that the fine mesh (element size $0.02a$) produced stress distributions that differed by less than 1% from coarser meshes, indicating that it was sufficiently refined. A convergence check was also carried out using the algorithm described in Sinclair et al. (2016), further confirming the robustness of the model.

3.1. Results and analysis of the finite length, common-edge contact

As mentioned before, each whole model behaves as a monolithic body with prescribed boundary conditions, independent of z. Therefore, through the analysis in Section 2.2, we expect that the stress field in plane strain, and in the mid-plane of the finite length problem will be the same for this geometry. Additionally, we aim to observe how the free end effect propagates by taking a 2D plane strain solution as a reference, and comparing it with the state of stress of the plane cross-section at each z co-ordinate.

The analysis of the FE results starts by extracting the contact pressure at the mid-plane and end-plane from the finite element experiments mentioned in Table 1. These contact pressures are then compared with the corresponding plane strain solution. In all three models of Table 1, it can be observed that the finite, common edge contact exhibits lower pressure at the free end than the reference plane strain solution, but at the mid-plane, the pressure profilescoincide, as expected.

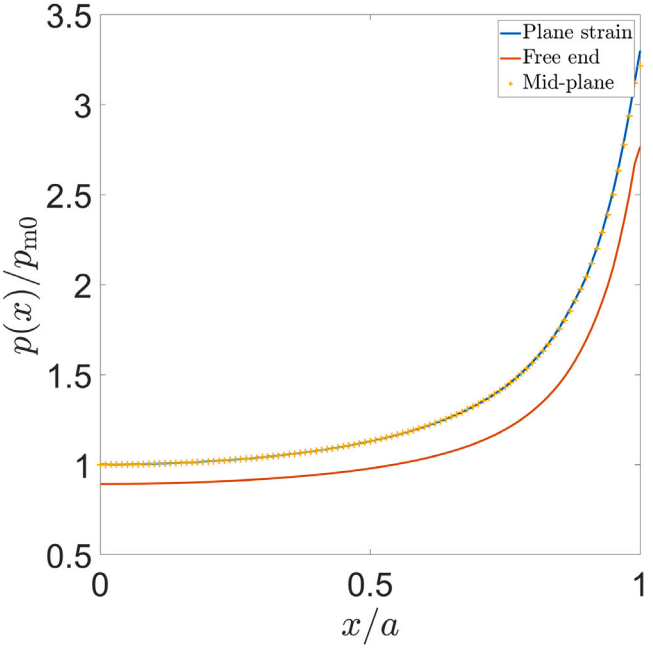

Fig. 6. Contact pressure comparison between the plane strain solution, the mid-plane and the free end-plane of a finite length, common edge contact: model P2000L100r2.5a7.5.

An example of this comparison, from model P2000L100r2.5a7.5, is shown in Fig. 6. Here, the mid-point contact pressure (minimum pressure) in the plane strain common edge contact is denoted by p_{m0} and this value is subsequently used to normalize $p(x)$ in all numerical experiments.

The analysis of FE results proceeds by extracting the direct stress component normal to the mid-plane, $\sigma_{zz}^{M}(x, y)$, and comparing with $\sigma_{zz}^{PS}(x, y)$, the plane strain solution. The latter is directly extracted from a plane strain finite element model. The comparison reveals that the difference between these two out-of-plane stresses is uniform in the x-y

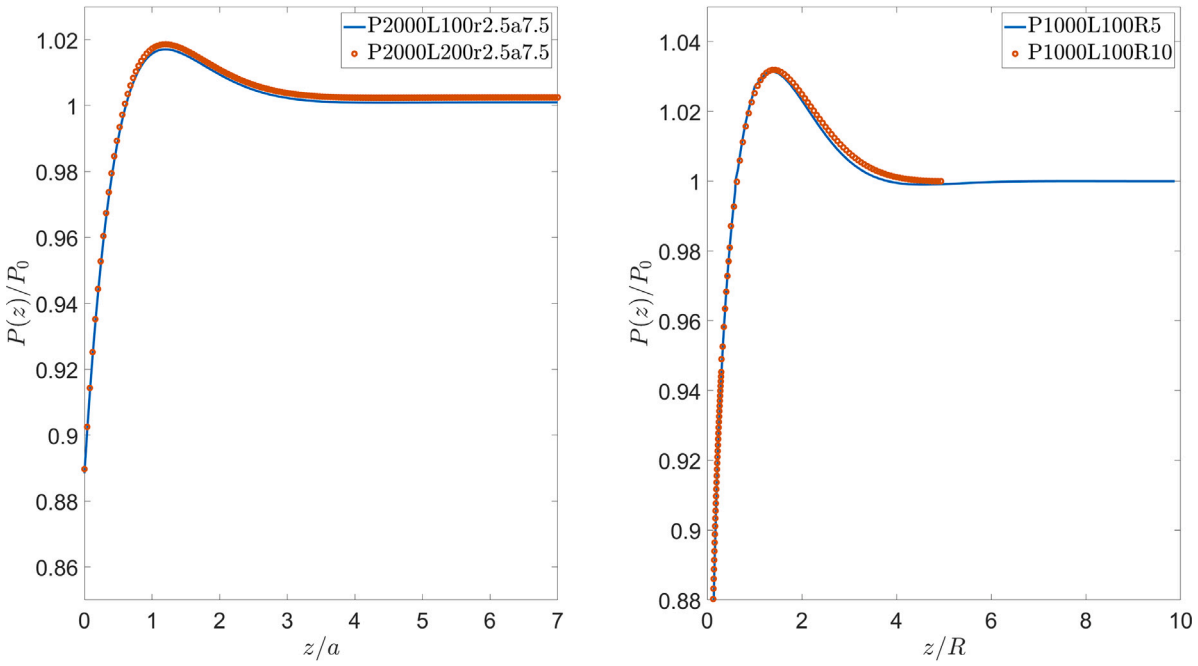

Fig. 7. The variation of $P(z)/P_0$ with z from different models: (a) finite length, common edge contact; results show similarity when z is normalized by **the contact half-width** a; (b) finite length, Hertzian contact, results show similarity when z is normalized by **the contact indenter radius** R.

plane, and the value of this difference agrees with the average provided by Eq. (2). This can be analytically expressed as

$$\sigma_{zz}^{\mathrm{a}} = \frac{1}{A_0}\int_{A_0}\sigma_{zz}^{\mathrm{PS}}(x,y)\,\mathrm{d}A_0 = \frac{\nu}{A_0}\int_{A_0}\sigma_{yy}^{\mathrm{PS}}(x,y)\,\mathrm{d}A_0 = \frac{\nu P_0 w}{A_0} \tag{11}$$

for the plane geometry shown in Fig. 5(a). The agreement validates the corrective solution proposed in Section 2.

The variation of contact force per unit length at each plane, $P(z)$, indicates how the applied load is distributed along the contact surface. Consequently, it can be used to evaluate the behavior of the transient region. $P(z)$ is defined as the integral of the contact pressure across the contact half-width, i.e.

$$P(z) = \int_{-a}^{a} p(x)\,\mathrm{d}x. \tag{12}$$

This quantity can be normalized by the applied force per unit length P_0; the quantity $P(z)/P_0$ is used to observe the decay of the end effect.

It can be anticipated that the end effect will propagate inward only for a limited distance. Determining this range in terms of the geometric length feature is one of the key objectives of this paper. A suitable candidate for the nondimensionalization of the length over which the end effect diminishes is the contact half-width, a (an alternative choice would be feature radius r).

Fig. 7(a) shows results from models P2000L100r2.5a7.5 and P2000L200r2.5a7.5. These two models have the same x-y plane geometry, differing only in their length, L. This verifies that the results are independent of L with $L \gg r, a$. These results also indicate that the length is divided into a transient region and a steady state region, with the transient region having length about $4a$. Note that Fig. 7(b) shows corresponding results from a Hertzian contact model, for later use.

The range of the end effect varies when the geometry in the x-y plane changes, as shown in Fig. 8, where the cross-section of the models is characterized by their a/r ratio. Note that $a/r \to \infty$ corresponds to the scenario where two identical blocks are pressed against each other, resulting in a contact patch that remains unchanged along the length. Consequently, in cases of common edge contact, a larger a/r ratio is expected to yield a smaller end-effect range. In simple terms, smaller grooved features produce a more confined transient region.

Numerous studies have demonstrated that the decay pattern of a self-equilibrating end effect follows an oscillating exponential function, see Horgan and Knowles (1983) and Toupin (1965). The data in Fig. 8 were found to fit an oscillating exponential function of the form

$$P(z)/P(0) = A\exp(-\lambda(z/a))\sin(\omega(z/a)+\phi)+1 \tag{13}$$

where λ is the decay constant, ω is the angular frequency of the oscillation and ϕ is a phase shift. Using the Levenberg–Marquardt nonlinear least squares fitting algorithm (Levenberg, 1944) (See Appendix for details), the following fitting functions were identified:

$$P(z)/P(0) = 0.562\exp(-0.944(z/a)) \times \sin(0.617(z/a)-0.612)+1 \quad \text{for } a/r=1 \tag{14}$$

$$P(z)/P(0) = 0.195\exp(-1.560(z/a)) \times \sin(0.983(z/a)-0.615)+1 \quad \text{for } a/r=3 \tag{15}$$

Both fitted curves show maximum error less than 0.1%. While the common edge contact is a simpler case than the target problem of Hertzian contact, the results given indicate the robustness and accuracy of our method to decompose the contact problem into a generalized plane strain case at the mid-plane and a corrective solution.

4. Finite length, Hertzian contact

We next proceed to study the frictionless, finite length, Hertzian contact, represented as two parallel frictionless identical cylinders pressed onto each other with their ends aligned, as shown in Fig. 9(a). The cylinders have length $2L$, radius $R \ll L$ and are pressed together by a uniform line force P_0. This is a type of convex contact, and hence will display a non-constant contact width, shown in Fig. 9(c). This model shares the same through-thickness (3D) effect with the cylinder on plane model. However, the current model is computationally efficient, being identical to a cylinder pressed against a rigid surface (Fig. 9(b)). Due to symmetry, only one-eighth of the 3D model is required. For all of the FE experiments, we take Poisson's ratio $\nu = 0.3$.

In computational experiments, it was observed that the contact pressure gradient in the length direction is very steep near the free

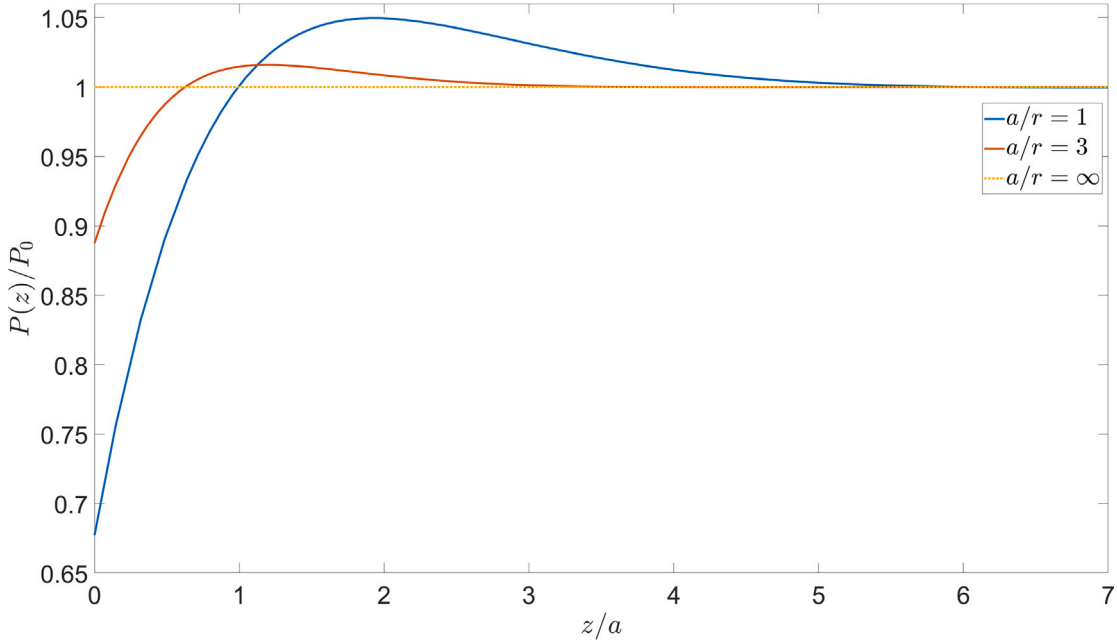

Fig. 8. Common edge contact: contact force per unit distribution of models with $a/r = 1, 3, \infty$.

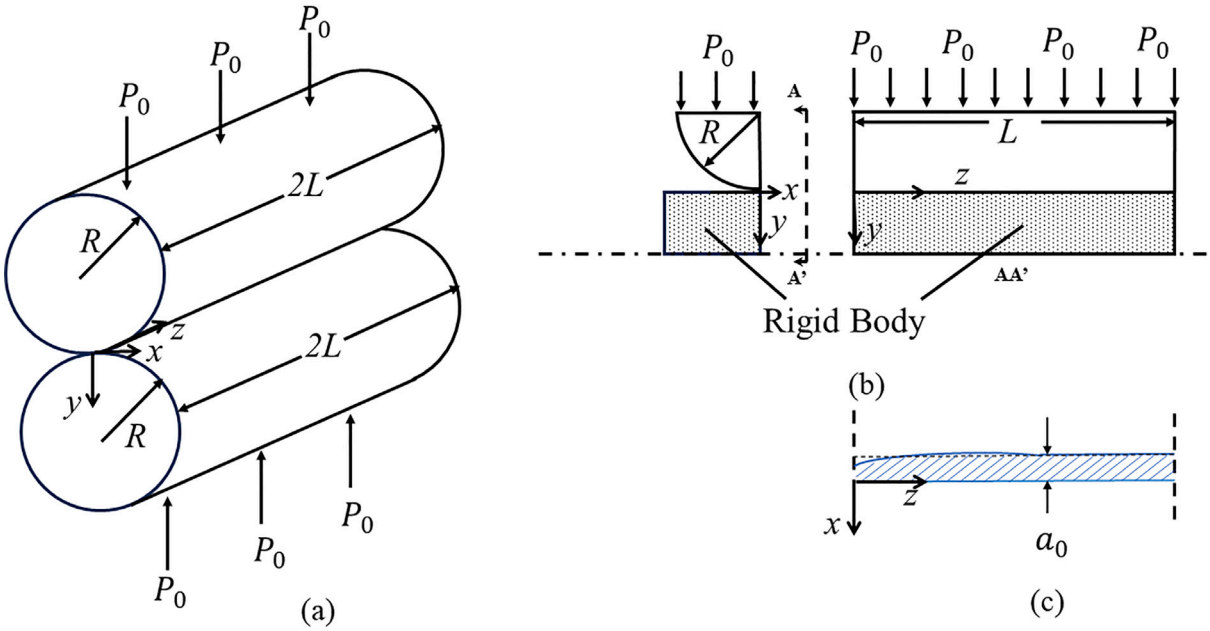

Fig. 9. (a) Frictionless, finite length, Hertzian contact, (b) FE model of finite length, Hertzian contact, (c) contact half-width distribution for the finite length, Hertzian contact.

end. Consequently, a finer mesh was used for this region. Another challenge with the mesh design is that, to maintain 'conformal' contact, the contact width needs to be small compared to the in-plane geometry. To accurately capture the contact pressure profile in such a small area, fine mesh is required for the region close to $y = 0$. The meshing strategy is illustrated in Fig. 10.

To control the variables involved in the numerical experiments systematically, eight different sets of numerical experiments with different loads P_0 (hence different contact half width in the plane strain case), different length L and different cylinder radius R were examined, see Table 2. The setup of finite element models is the same as that in common-edge contact models, and the mesh sensitivity shows that the fine mesh (element size $0.005R$) produced stress distributions that differed by less than 1% from coarser meshes.

4.1. Results and analysis of finite, Hertzian contact

The solution for a plane strain Hertzian contact, with indenter radius R and force per unit length P_0 is used as a reference. Its contact half-width, a_0, and pressure profile $p(x)$ are:

$$a_0^2 = \frac{4(1-\nu^2)RP_0}{\pi E} \tag{16}$$

$$p(x) = -\frac{2P_0}{\pi a_0}\sqrt{1-(x/a_0)^2} = p_{m0}\sqrt{1-(x/a_0)^2} \tag{17}$$

where p_{m0} is the maximum contact pressure.

We begin by comparing the contact pressures at the mid-plane and at the free-end to the reference solution. Unlike the common edge contact, superposition of load-cases is not available because the contact pressure is non-linearly related to load. Instead, the methods

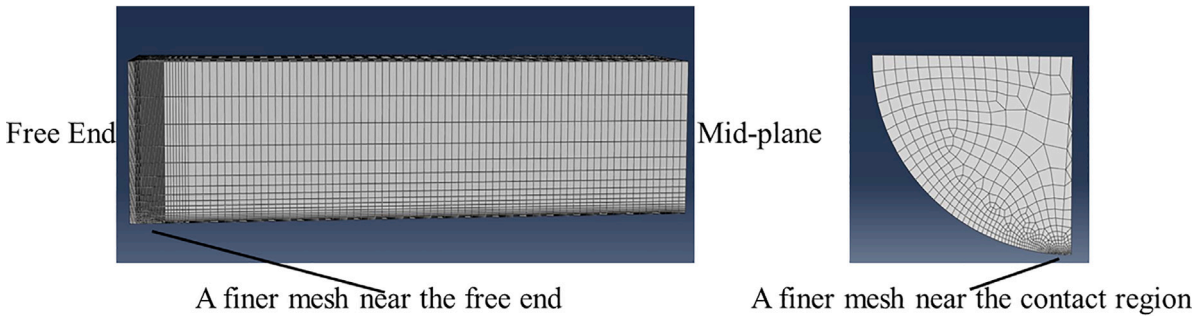

Fig. 10. Finite element mesh for the finite length, Hertzian contact.

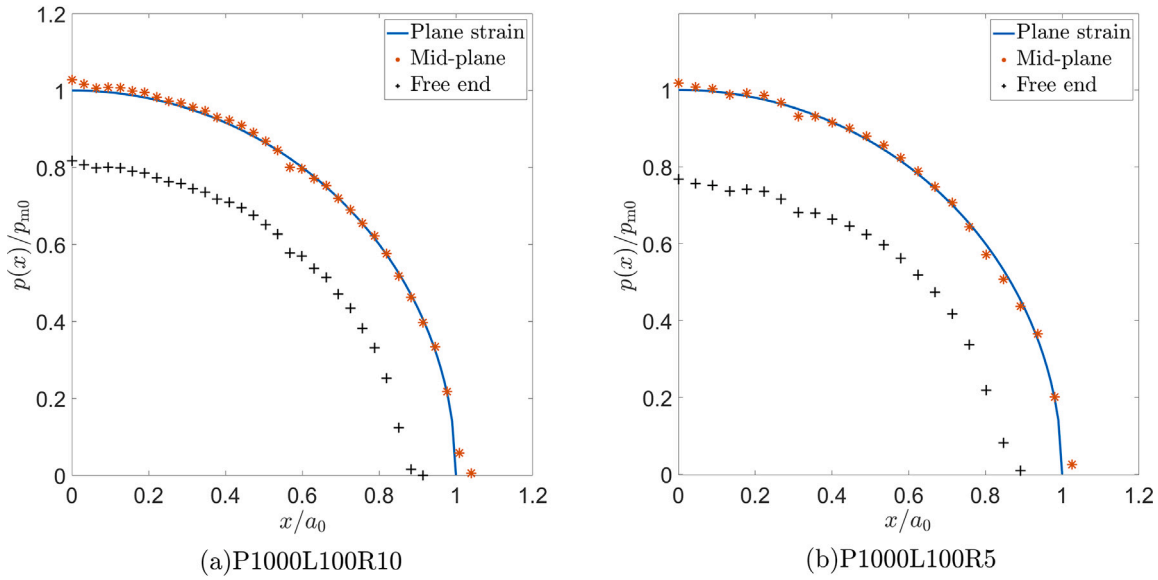

Fig. 11. Contact pressure comparison between the plane strain analytical solution and the FE calculation at the mid-plane and free-end of a finite length, Hertzian contact.

Table 2
FE model parameters for Hertzian contact models.

Hertzian contact models			
Model code	P_0 [MPa mm]	L [mm]	R [mm]
P2000L100R5	2000	100	5
P1000L100R5	1000	100	5
P2000L100R10	2000	100	10
P1000L100R10	1000	100	10
P2000L100R2.5	2000	100	2.5
P1000L100R2.5	1000	100	2.5
P2000L200R2.5	2000	200	2.5
P1000L100R2.5	1000	200	2.5

of Section 2.2 are applied. Since the two bodies are uncoupled and elastically similar, we anticipate, from the discussion in Section 2, that the contact pressure profile at the mid-plane will be similar to that of the plane strain contact. To verify this expectation, the contact pressure distributions at the mid-plane and the free-end were extracted for all eight models and compared with the plane strain solution. Two examples of such comparisons, from models P1000L100R10 and P1000L100R5, are shown in Fig. 11.

In Fig. 11, the FE data are normalized by the mid-point (maximum) pressure p_{m_0}; spatial position is normalized by the analytical contact half-width a_0. The FE data have limited accuracy due to discontinuity at the contact interface, however, it is evident that the mid-plane data closely matches the plane strain case. At the free end, both the contact pressure and the contact half-width are smaller than those observed in plane strain, indicating the presence of an end-effect. The contact pressure distribution near the free-end is difficult to model accurately due to steep pressure gradients and slight mis-alignment of the two contacting bodies at the free end. Nevertheless, estimations of the stress state close to the end can be made by fitting an end-effect decay equation, as used in Section 3.

The decay of the end effect has been discussed in Section 2.2. This shows that the stresses of the finite length contact problem can be recovered by adding $-\sigma_{zz}^{\mathrm{PS}}(x,y)$ to both ends of the plain strain prismatic contact, so that the free end boundary condition is achieved. The expression of $\sigma_{zz}^{\mathrm{PS}}(x,y)$ can be evaluated using the Muskhelishvili potential (Muskhelishvili, 1953), as discussed by Hills et al. (2013).

The propagation of $-\sigma_{zz}^{\mathrm{PS}}(x,y)$ along the cylinders is subject to Saint-Venant's principle. This implies that in the finite length, Hertzian contact, the out-of-plane stress $\sigma_{zz}(x,y,z)$ changes from zero at the free end to $\sigma_{zz}^{b}(x,y)$ at the mid-plane, where $\sigma_{zz}^{b}(x,y)$ is defined in Eq. (3). Furthermore, the uniform stress, σ_{zz}^{a}, defined as the difference between the plane strain solution $\sigma_{zz}^{\mathrm{PS}}(x,y)$ and the mid-plane solution $\sigma_{zz}^{b}(x,y)$ can be expressed as:

$$\sigma_{zz}^{\mathrm{a}} = \frac{1}{A_0}\int_{A_0}\sigma_{zz}^{\mathrm{PS}}(x,y)\,\mathrm{d}A = \frac{\nu}{A_0}\int_{A_0}\sigma_{yy}^{\mathrm{PS}}(x,y)\,\mathrm{d}A$$

$$= \frac{\nu}{A_0}\int_0^R\int_0^{\sqrt{R^2-y^2}}\sigma_{yy}^{\mathrm{PS}}(x,y)\,\mathrm{d}x\mathrm{d}y = \frac{\nu R P_0}{2A_0} = \frac{2\nu P_0}{\pi R}$$

or

$$\frac{\sigma_{zz}^{\mathrm{a}} R}{P_0} = \frac{2\nu}{\pi} \tag{18}$$

For $\nu = 0.3$ this value is about 0.191.

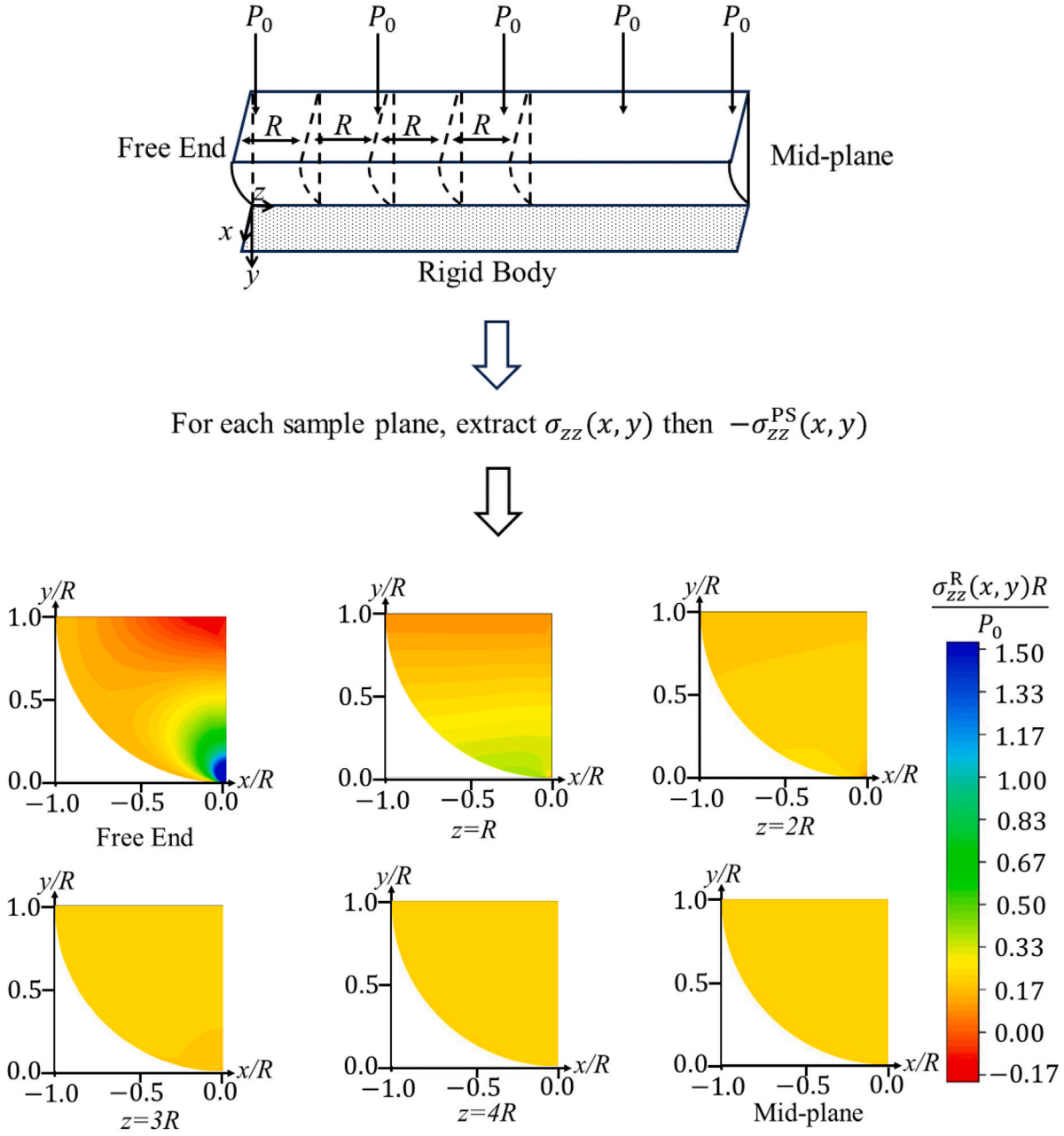

Fig. 12. Illustration of the modified through-thickness stress distribution, σ^{R}, at sample planes in a finite length, Hertzian contact.

To visualize the end-effect propagation, the resultant stress, $\sigma_{zz}^{R}(x,y) = \sigma_{zz}(x,y) - \sigma_{zz}^{PS}(x,y)$, was computed using the FE data, with the plane strain solution calculated using the Muskhelishvili potential. The resultant stress $\sigma_{zz}^{R}(x,y)$ is expected to match the plane strain corrective stress $-\sigma_{zz}^{PS}(x,y)$ at the free end, and decay to a uniform stress distribution, $-\sigma_{zz}^{a}$ in the steady state region. Fig. 12 shows the resultant stress on planes located at $z = 0$, R, $2R$, $3R$, $4R$ and at the mid-plane ($z = 10R$) of model P1000L100R10. As expected, the stress converges to a uniform distribution, with normalized magnitude about equal to 0.19, matching the prediction of Eq. (18).

Note that, unlike the common edge contact, the half-width of the Hertzian contact is not constant along the length. Thus it is not a suitable dimension for normalization of the z co-ordinate. The only remaining geometric dimension is the indenter radius R. From the FE results, it is found that all eight models show similar forms of $P(z)/P_0$ when z is normalized as z/R; example results for models P1000L100R5 and P1000L100R10 were shown in Fig. 7(b). The calculation of $P(z)/P_0$ was performed using Eq. (12) via Simpson's rule with a step size of approximately $a_0/40$. Fig. 7(b) also clearly indicates that the length divides into a transient region and steady state region, with the transient region covering about $5R$ of the length.

The $P(z)$ data were processed to remove two sources of error. Firstly, steep pressure gradients close to the free end were not captured well by the FE model; the affected points were excluded from subsequent curve fitting. Secondly, quadrature error from Simpson's rule resulted in the steady state $P(z)/P_0$ not settling to unity, so the data were scaled to force $P(z) = P_0$ at $z = L$. Fig. 13 shows a comparison between the raw data and the post-processed data.

The normalized and adjusted data were fitted to an oscillating exponential decay using the Levenberg–Marquardt algorithm (see Appendix) resulting in

$$P(z)/P(0) = -0.289\exp(-1.245(z/R))\sin(0.864(z/R) + 2.611) + 1 \qquad (19)$$

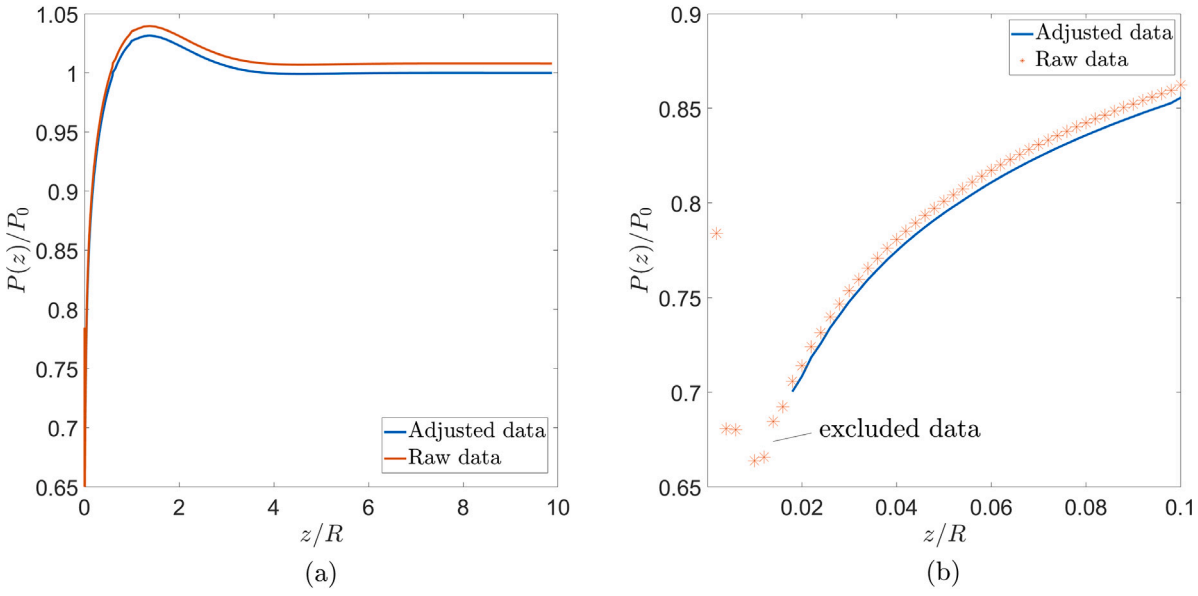

Fig. 13. Illustration of the raw data and the post-processed data of normalized contact force per unit length: (a) scale $z/R \in [0 \quad 10]$; (b) scale $z/R \in [0 \quad 0.1]$.

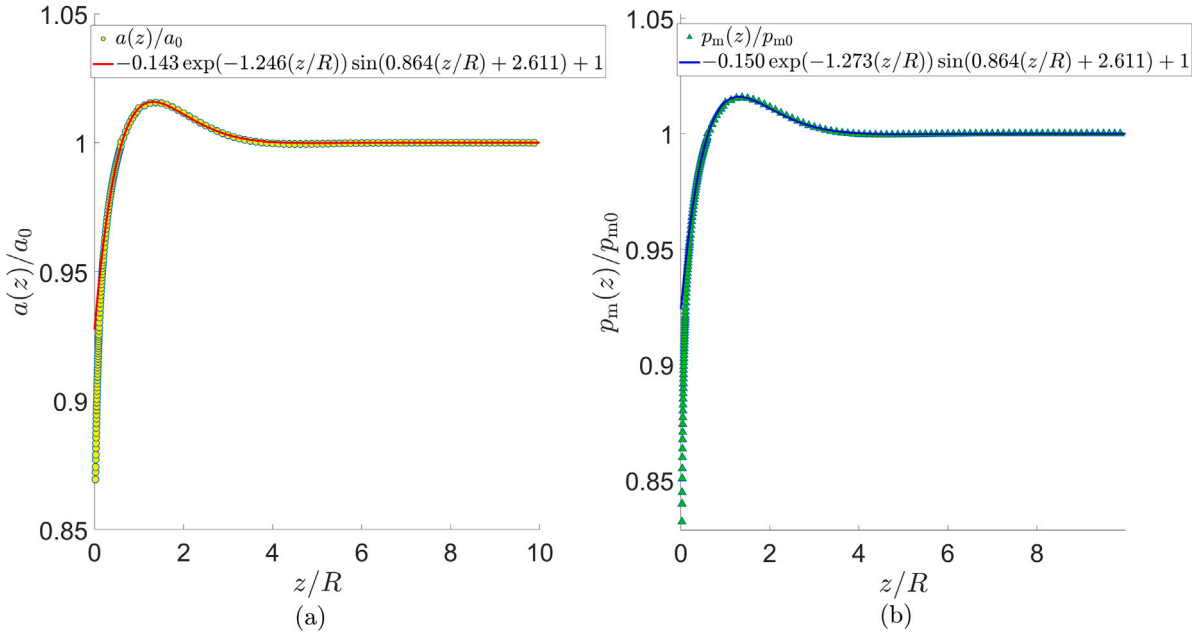

Fig. 14. Propagation of (a) contact half-width and (b) maximum contact pressure along the length of the contact.

with maximum error smaller than 0.1% for all $z/R > 0.06$. The contact half-width $a(z)$ could not be directly identified from the FE data due to limited mesh resolution. However, using the maximum contact pressure, it was possible to recover the contact half-width, noting the square root bounded distribution of contact pressure, i.e.

$$P(z) = p_{\mathrm{m}}(z)\int_{-a(z)}^{a(z)}\sqrt{1-(x/a(z))^2}\,\mathrm{d}x = \frac{\pi p_{\mathrm{m}}(z)a(z)}{2} \tag{20}$$

where $p_{\mathrm{m}}(z)$ is the maximum contact pressure at position z along the length. Hence

$$a(z) = \frac{2P(z)}{\pi p_{\mathrm{m}}(z)} \tag{21}$$

The contact half-width and maximum contact pressure are plotted as functions of z along with fitted oscillatory exponential decays in Fig. 14(a) and (b). The curve fits have the form

$$a(z)/a_0 = -0.143\exp(-1.246(z/R))\sin(0.864(z/R)+2.611)+1 \tag{22}$$

for the contact half-width, and for the maximum contact pressure

$$p_{\mathrm{m}}(z)/p_0 = -0.150\exp(-1.273(z/R))\sin(0.864(z/R)+2.611)+1 \tag{23}$$

Note that the oscillatory frequencies and phase shifts are closely matched between Eqs. (19), (22) and (23); this is expected because they are produced by the transient of the same end effect.

From Fig. 14, it can be observed that the transient region extends approximately to $5R$, and the contact pressure reaches a maximum at $z/R = 1.3$. The maximum contact force per unit length is $1.03P_0$ and the maximum contact pressure is $1.02p_{\mathrm{m0}}$. The above findings have generality. The decay functions can also be extrapolated to $z = 0$ indicating that the force per unit length at the free end is about $0.86P_0$ while the free end contact has a maximum pressure of $0.92p_{\mathrm{m0}}$ and a contact half-width of $0.93a_0$.

It is important to note that when applying the above results to a general Hertzian contact, the characteristic length for contact propagation should be the radius of the smaller contact body according to St. Venant's principle. Therefore, under the conditions of uncoupled Hertzian contact, or Hertzian contact with $\gamma = 0$, the transient region lasts approximately $5R_s$, where R_s is the smaller radius.

Noting that for Hertzian contacts, typically, $R \gg a$, this means that the penetration of the end effect in the length dimension is much greater that the contact width. In this respect the Hertzian contact differs qualitatively from the common edge contact, where the end effect typically penetrates less than $5a$ along the length. The numerical models also indicate that Saint-Venant's principle relates to a geometric feature size that is independent of load: in the Hertzian contact the load-dependent contact half-width does not affect the decay of the end-effect.

5. Conclusion

This paper analyzes the free-end effects found in prismatic contacting bodies. Two types of contacts were used as examples: a common edge contact and a Hertzian contact. Numerical experiments confirmed that the free-end effect is characterized by a transient region, governed by an oscillatory exponential decay of contact pressure. Towards the mid-plane, a steady-state is reached, corresponding to a modified plane strain solution of the corresponding 2D problem. The paper clearly shows observations of the pressure distribution and the end-effect, with results that have generality for the Hertzian case. The transient region of the Hertzian case has been found to be about 10 times the inverse curvature of the cross-sectional geometry.

Additionally, this work analyzes the steady-state portion of the finite length problem, as observed at the mid-plane. The mid-plane stress state can be recovered by imposing a uniform anti-plane stress onto the plane strain solution. This uniform stress corresponds to the average through-thickness stress in the plane strain case. In the case of a monolithic prismatic body (i.e. not a contact) of sufficient length, the in-plane stress field of the mid-plane is the same as that in the plane strain condition. In a finite length contact problem, the above statement still holds if the two contacting bodies are uncoupled or the material constant $\gamma = 0$.

Finally, expressions for the decay of the end effect were provided. This enables the propagation of the force per unit length, the maximum contact pressure, and the contact half-width to be predicted. The paper provides insight and understanding potentially valuable in the analysis of contact fretting, and prismatic contacts found in a variety of engineered components.

CRediT authorship contribution statement

Yifeng Chen: Writing – review & editing, Writing – original draft, Resources, Methodology, Investigation, Formal analysis, Data curation, Conceptualization. **David A. Hills:** Supervision. **John E. Huber:** Supervision. **Lifeng Ma:** Supervision.

Declaration of competing interest

The authors declared no potential conflicts of interest with respect to the research, authorship, and/or publication of this article.

Acknowledgment

Special thanks are given to Professor J.R. Barber from the University of Michigan for his kind suggestions on the exponential decay pattern of the end-effect.

Appendix. Nonlinear fitting algorithm

This appendix outlines the algorithm used to fit the numerical data. The expected form is an oscillatory exponential decay given by:

$$y = A\exp(-\lambda x)\sin(\omega x + \phi) + 1,$$

where y is the dependent variable, x is the independent variable, and A, λ, ω, and ϕ are the parameters to be estimated.

This can be expressed as $y = f(x;\Theta)$, where $\Theta = [A, \lambda, \omega, \phi]$ represents the vector of parameters to be estimated. The objective of the fitting process is to find the parameter values that minimize the difference between the observed data points and the values of function f. This is typically achieved by minimizing a cost function, defined as the sum of squared errors (SSE):

$$\mathrm{SSE}(\Theta) = \sum_{i=1}^{n}[y_i - f(x_i;\Theta)]^2,$$

where y_i and x_i are the observed values of the dependent and independent variables, respectively, and n is the number of observations.

The fitting process involves an optimization algorithm that iteratively adjusts the parameters Θ to minimize the SSE. The Levenberg–Marquardt algorithm (Levenberg, 1944) is a damped least square optimization algorithm that interpolates between the Gauss–Newton algorithm and gradient descent, using

$$\Theta_{new} = \Theta_{old} + (J^T J + \gamma \cdot \mathrm{diag}(J^T J))^{-1} J^T [y - f(z;\Theta_{old})]$$

where J is the Jacobian matrix of partial derivatives of f with respect to the parameters, γ is a damping factor that adjusts the algorithm's behavior between the Gauss–Newton and gradient descent methods, and $\mathrm{diag}(J^T J)$ is the diagonal matrix of $J^T J$.

The fitting process was implemented using the `curve_fit` function in Python, using $\Theta = [1, 1, 1, 1]$ as an initial guess and iterating the Levenberg–Marquardt algorithm until a stable Θ is found.

Data availability

No data was used for the research described in the article.

References

Barber, J.R., 2006. Three-dimensional elasticity problems for the prismatic bar. Proc. R. Soc. A: Math. Phys. Eng. Sci. 462 (2070), 1877–1896.

Blades, L., Truelove, J.P., Paynter, R., Hills, D.A., 2023. Experimental investigation of the effects of load path on the life of fretting fatigue contacts. Tribol. Int. 188, 108858.

De Pannemaecker, A., Fouvry, S., Buffiere, J.Y., Brochu, M., 2018. Modelling the fretting fatigue crack growth: From short crack correction strategies to microstructural approaches. Int. J. Fatigue 117, 75–89.

Hills, D.A., Nowell, D., Sackfield, A., 2013. Mechanics of Elastic Contacts. Elsevier.

Horgan, C.O., Knowles, J.K., 1983. Recent developments concerning Saint-Venant's principle. In: Hutchinson, J.W., Wu, T.W. (Eds.), Advances in Applied Mechanics. vol. 23, Elsevier, pp. 179–269.

Johnson, K.L., 1987. Contact Mechanics. Cambridge University Press.

Levenberg, K., 1944. A method for the solution of certain non-linear problems in least squares. Quart. Appl. Math. 2 (2), 164–168.

Love, A.E.H., 2013. A Treatise on the Mathematical Theory of Elasticity. Cambridge University Press.

Muskhelishvili, N.I., 1953. Some Basic Problems of the Mathematical Theory of Elasticity. Noordhooff, Groningen.

Roark, R.J., 1975. Formulas for Stress and Strain. McGraw-Hill.

Sinclair, G.B., Beisheim, J.R., Roache, P.J., 2016. Effective convergence checks for verifying finite element stresses at two-dimensional stress concentrations. J. Verif. Valid. Uncertain. Quantif. 1 (4), 041003.

Toupin, R.A., 1965. Saint-Venant's principle. Arch. Ration. Mech. Anal. 18 (2), 83–96.

Truelove, J.P., Hills, D.A., Blades, L.E., 2023. Flat and rounded contacts: Modelling the effect of a moment with application to fretting fatigue tests. J. Strain Anal. Eng. Des. 58 (2), 91–97.